Computational Condensed Matter 40 (2024) e00927

Contents lists available at ScienceDirect

Computational Condensed Matter

journal homepage: www.elsevier.com/locate/cocom

Analysis of Na_2CuP ternary semiconductor compound for optoelectronic application by first-principles methods using GGA and mGGA functionals

Robinson Musembi [a,*], Mwende Mbilo [a], Martin Nyamunga [a], John Kachila [a,b]

[a] Monolith Research Group, Department of Physics, Faculty of Science and Technology, University of Nairobi, P.O. Box 30197, 00100, Nairobi, Kenya
[b] Department of Physics, Mbeya University of Science and Technology, P.O. Box 131, Mbeya, Tanzania

ARTICLE INFO

Keywords:
DFT
metaGGA
Ternary compounds
Zintl phase
Optoelectronics

ABSTRACT

An ab initio study of Zintl Na_2CuP ternary semiconductor compounds was carried out by applying first-principles methods to calculate the structural, electronic, elastic, mechanical, and optical properties using generalised gradient approximation (GGA) and metaGGA exchange-correlation functionals. The bandgap was determined to be 0.7523 eV and 0.7848 eV using GGA with Wu-Cohen and Perdew-Burke-Ernzerhof (PBE) functionals, respectively. The bandgap was re-approximated using the more accurate metaGGA functionals as 1.078 eV and 1.084 eV using the Tran-Blaha modified Becke Johnson exchange and correlation functional (TB-mBJ) and the strongly constrained and appropriately normed (SCAN) functional, respectively. The projected density of states using the GGA revealed that the conduction band formation was mainly by Cu 2*p*, P 2*p*, and Na 2*s* orbitals with the rest of the orbitals making a minor contribution. In contrast, the valence band formation was mainly formed by Cu 3*d* and P 2*p*, with the rest of the orbital playing a minor role in the formation. The material was found to be mechanically brittle with a covalent bond, which is a characteristic of Zintl-phased materials. The Na_2CuP material was also observed to have a strong absorption coefficient between 1.15 eV and 15 eV, a characteristic suitable for photovoltaic applications.

1. Introduction

The world has developed to a level where numerous devices being used are fabricated using different types of materials. The semiconductor industry has played a key role in developing various devices, particularly for optoelectronic applications. Photovoltaics (PVs) are emerging as one of the best alternative optoelectronic devices as green energy sources, and the vast majority of PVs are made of single-crystal silicon absorbers. Despite their popularity, silicon-based solar cells have several drawbacks. These include complex manufacturing processes that make them uneconomical [1]; the small light absorption coefficient of silicon near its bandgap, which limits its potential for photon capture, limiting the efficiency of silicon solar cells [2]; and their brittleness and hardness, which makes them unsuitable for use in flexible solar cells [3]. These limitations have prompted extensive theoretical and experimental research to identify potential replacement materials that can be used as absorbers to capture electricity from sunlight.

An alternative to single-crystal silicon materials in the photovoltaic (PV) market is the thin-film technology, which currently accounts for a negligible proportion of the market. Ternary chalcogenide materials are among the earliest materials used in thin-film technology, with relatively good stability [4]. These materials can be categorised as chalcopyrite or pnictide. Despite their use in thin-film technology, some of them are hindered by various issues, including the use of scarce elements, such as In, Ga, or Te [4], or toxic elements, such as Pb or Cd [5,6], as well as long-term stability problems, such as those affecting halide perovskites.

To solve these thin-film technology problems, pnictides have been explored as alternative absorbers. These pnictides exist in Zintl phases featuring group V_A anions, including phosphorus, arsenic, antimony, and bismuth [7,8]. In addition to pnictides, these compounds have been studied using the Zintl concept, which is a well-established method in the field of solid-state chemistry. This approach employs electron-counting rules to elucidate the behaviour of numerous Zintl compounds [9]. These compounds have attracted considerable interest from researchers in recent years, especially for thermoelectric applications. Zintl-phased compounds can not only find applications in thermoelectric but also in the optoelectronic industry, where they find applications in diode lasers, detectors, terahertz devices, as well as in

* Corresponding author.
E-mail address: musembirj@uonbi.ac.ke (R. Musembi).

https://doi.org/10.1016/j.cocom.2024.e00927
Received 26 April 2024; Received in revised form 9 June 2024; Accepted 10 June 2024
Available online 13 June 2024

photovoltaics [10,11].

Researchers are engaged in exploring alternative materials to replace silicon in solar cells, focusing on inorganic pnictides composed of earth-abundant elements [12]. Among these inorganic pnictide materials, alkali metal pnictogens have emerged as a promising class of materials for solar absorption owing to their anticipated optoelectronic and mechanical properties. Jayalakshmi et al. [13] conducted a study on the density functional theory (DFT) properties of caesium phosphide (Cs_3P) and its potential for optoelectronic applications. The study revealed that Cs_3P exhibits an optimal bandgap of 0.952 eV, making it a suitable candidate for optoelectronic devices. Furthermore, an investigation of the thermoelectric properties of Cs_3P showed that it possesses a high power factor, which corresponds to a high thermoelectric efficiency, suggesting its potential for photothermal conversion. Consequently, Cs_3P is considered a promising material for use in solar-cell technology.

In addition to binary alkali metal phosphides, ternary alkali metal-based phosphides have been studied as potential photovoltaic materials. These compounds are composed of alkali metals, transition metals, and phosphorus [11]. Computational methods have been extensively used to investigate ternary alkali metal-based phosphides, particularly those containing potassium elements. For example, $K_3Cu_3P_2$, $K_3Ni_3P_2$, K_4ZnAs_2, K_4ZnP_2, K_4CdP_2, K_4HgP_2, Na_4HgP_2, and $K_3Cu_3P_2$ have been studied for potential applications in optoelectronics and photovoltaics [14–18]. These compounds exhibit suitable optical properties such as an appropriate bandgap that matches the solar spectrum, making them suitable for use as solar absorbers. Furthermore, sodium-based ternary-based phosphides have been investigated. For instance, the mechanical stability of Na_2CuP was predicted by DFT using the generalised gradient approximation (GGA) with the Perdew–Burke–Ernzerhof (PBE) functional [19]. The optical bandgap of Na_2CuP was previously computed using the local density approximation (LDA) and GGA [11, 20], respectively. Finally, computational screening of the carrier lifetime and structural and electronic properties of Na_2CuP for application as a solar absorber was performed using the PBE + Heyd (Scuseria) Ernzerhof approach [21].

Previous research on Na_2CuP has primarily focused on its electronic, mechanical, and optical properties utilising LDA, GGA-PBE, and PBE + HSE approximations and correlation functionals. However, these methods, including LDA, GGA approximations, and the PBE functional, have been found to underestimate the bandgap and lead to incorrect calculations of the defect transition levels [21,22]. Therefore, our work focused on an ab initio study conducted to investigate the structural, electronic, elastic, mechanical, and optical properties of Na_2CuP using SCAN and TB-mBJ functionals, and the results were compared with those obtained using GGA-PBE for potential photovoltaic applications. In addition to this, the Wu-Cohen exchange correlation functional based on generalised gradient approximation exchange and correlation potential has been utilised because of its strength for the best approximation of thermodynamic properties of solid state materials, and further to buttress the bandgap approximation, machine learning approach was also brought onboard.

2. Computational methods

All calculations in this work were performed using the plane wave self-consistent field, Pwscf, method as implemented in the Quantum ESPRESSO computational code which applies the ab initio techniques of the density functional theory [23,24]. The generalised gradient approximation was used for estimating the exchange-correlation potential for the baseline study using the Perdew–Burke–Ernzerhof exchange-correlation functional GGA-PBE [25]. For higher accuracy in the DFT ladder, SCAN and Tran-Blaha modified Becke-Jonhson meta-GGA's were used as exchange correctional functional after the baseline study, also numerical calculations using machine learning were performed. The machine learning calculations were done using a web-based tool offered by the materials database www.aflowlib.org where a POSCAR input file describing the structure of the material is uploaded [26–29]. The interactions between the valence electrons and ionic core were described using the pseudopotential method. Two types of pseudopotentials were used in this work: the Kresse–Joubert projector augmented plane wave [30], scalar relativistic with nonlinear core correction, and norm-conserving pseudopotentials for the GGA and *meta*-GGA calculations, in which the valence electrons for the Na_2CuP ternary compound are Na [Ne] $3s$, Cu [Ar] $3d^{10}4s$, and P [Ne] $3s^23p^3$, respectively. The first irreducible Brillouin zone (BZ) sampling was performed using the Monkhorst–Pack sampling scheme, where the k-point mesh for the BZ used during sampling was $9 \times 9 \times 9$ with an offset of 1. Similar values of the k-point were used during further optimisation, including the kinetic energy cut-off set at 60.0 Rydberg while the charge density cut-off was set to be calculated automatically. The lattice parameter, a_o, as a function of total energy and variable cell relaxation, was optimized at 0.0 applied pressure following the Broyden–Fletcher Goldfarb–Shanno (BFGS) algorithm. During optimisation and any subsequent calculation, the convergence tolerance was set at 2.0×10^{-9} Ry.

3. Results and discussion

3.1. Structural properties

The Na_2CuP ternary compound crystallises into an orthorhombic crystal system while the lattice adopts the same structure with space group *cmcm* number 63, the lattice parameters for the conventional crystal systems are $a = 6.92$ Å, $b = 8.62$ Å, $c = 5.18$ Å, $\alpha = \beta = \gamma = 90^\circ$ and the volume 309.16 Å^3, the crystal system is shown in Fig. 1.

In the Na_2CuP ternary compound, the elements have the following Wyckoff positions. The Cu element occupies the 4b Wyckoff position at Cu(½, 0, ½), while the P occupies the 4c Wyckoff position at P(0.760502, 0, ¾), and lastly, the Na is 8g Wyckoff position at Na(0.357228, 0.327362, ¼). The lattice parameters of the Na_2CuP compound were optimized by fitting the volume against total energy in the Birch-Murnaghan equation of state given in Equation (1) was used to compute the optimized values as tabulated in Table 1. The fitted values are as shown in Fig. 2.

$$E(V) = E_o + \frac{B}{B'(B'-1)}\left[V\left(\frac{V_o}{V}\right)^{B'} - V_o\right] + \frac{B}{B'}(V - V_o) \quad (1)$$

where in Equation (1), E_o, B, B′, V, and V_o are respectively, the optimum value of total energy, the bulk modulus, the pressure derivative of bulk modulus, the total unit cell volume, and the optimized unit cell volume. The results are given in Table 1. It can be observed that the lattice parameters a_o were in good agreement with the experimental

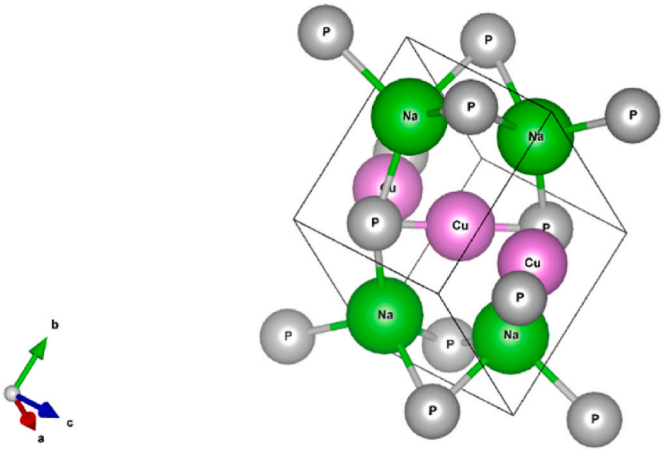

Fig. 1. Primitive crystal structure of Na_2CuP ternary compound.

Table 1
Computed ground-state lattice parameters, bulk modulus, equilibrium volumes, and enthalpies of formation of Na_2CuP ternary compound using GGA-PBE and GGA-WC functionals.

	Lattice parameter a_o (a.u)	Bulk modulus B_o GPa	Equilibrium volume $(a.u)^3$	Enthalpy of formation ΔH_f (Ry)
GGA-PBE	16.3821	43.7	1073.13	−974.48
GGA-WC	16.2029	47.3	1038.31	−970.42
Experiment	16.3981 [31]			

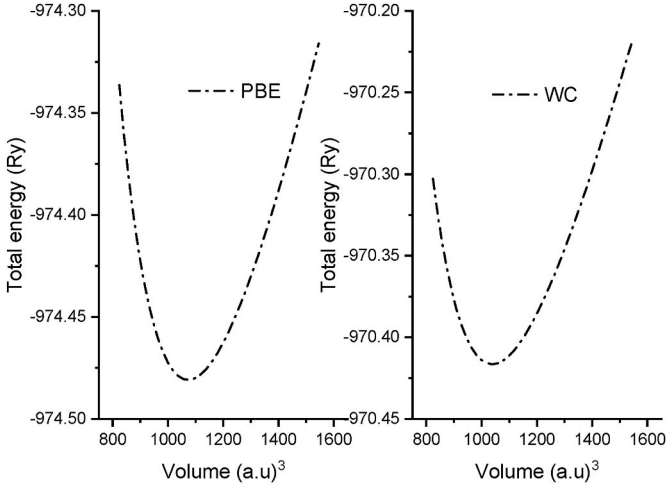

Fig. 2. The PBE-GGA and WC-GGA Birch-Murnaghan fitting for total energy and as a function of crystal lattice volume.

value of 16.3981 a.u. [31].

3.2. Electronic properties

To determine the properties of a material, including its conductivity, magnetism, and optical properties, it is important to understand its electronic structural properties. The band structure of the material helps to identify the allowed quantized energy levels for the electrons to occupy. The valence band represents a region of tightly bound electrons which are not available for electrical conduction, whereas the conduction band contains free electrons and is available for electrical conduction. The gap between the valence band and conduction band, known as the bandgap, helps determine whether a material is a conductor, semiconductor, or insulator. Other properties derived from studying the electronic structure include the Fermi level energy, density of states, and projected density of states. The electronic properties of the Na_2CuP ternary compound were studied using the PBE-GGA, WC-GGA, SCAN-mGGA, and TB-mBJ-mGGA functionals, and the results are shown in Fig. 3(a)–(d).

All calculations were performed along the Γ-X-S-R-A-Z-Γ-Y-X-A-T-Y-Z-T high-symmetry points in the Brillouin zone. The band diagrams were plotted using the range −5 eV–6 eV for energy minima and maxima, respectively, and the Fermi level at 0 eV. In Fig. 3(a)–(b), the calculated band structures reveal that the material is an indirect bandgap semiconductor with the valence band maxima (VBM) located at the X symmetry point and the conduction band minima (CBM) located at the Γ symmetry point. The calculated bandgaps for the materials were 0.7848 and 0.7523 eV for the PBE-GGA and WC-GGA functionals, respectively. It is worth noting that these two functionals significantly underestimate the bandgap of semiconductor materials; therefore, metaGGA functionals were used because they can estimate the bandgap closer to the experimental values. Two types of *meta*-GGA functionals were used to validate the values obtained from either of them. In electronic structure calculations, the density of states calculations describes the distributions of energy levels available for electron occupation in a material, while on the other hand, the projected density of states gives the understanding of how the electronic states are distributed among different atomic orbitals. The projected density of states calculations were performed to support the results obtained from the band structure calculations. The PBE-GGA shows that the conduction band formation was mainly formed by Cu 2*p*, P 2*p*, and Na 2*s* orbitals, with the rest of the orbitals making a minor contribution, while the valence band formation was mainly by Cu 3*d* and P 2*p*, with the rest of the orbital playing a minor role in the formation. A similar observation was made when Wu-Cohen functionals were used. The results obtained from the projected density of states were noted to corroborate those obtained for band structure calculations in terms of the size of the bandgap and the position of the Fermi level, supporting the accuracy of the results.

The calculations for the band structure using metaGGA are given in Fig. 3(c) and (d), which show the results obtained using the SCAN functional and Tran-Blaha-modified Becke-Johnson functionals, respectively. The bandgaps obtained using SCAN and TB-mBJ were 1.084 eV and 1.078 eV, respectively. The band structures obtained using the mGGA functionals are plotted without the respective projected density of states because the pseudopotentials used in this case do not have orbitals to project to. A further calculation using machine learning was performed giving 0.92 eV, a value which was between GGA and mGGA calculations. The close similarity in the bandstructure shows a characteristic isotropy in the electronic structure properties [32,33]. The calculated values are shown inTable 2.

3.3. Mechanical and elastic properties

The Na_2CuP compound assumes an orthorhombic crystal structure; In this structure, the elastic tensor has the lowest symmetry and highest number of independent elastic constants. The stiffness matrix has nine constants which are unrelated to each other, namely C_{11}, C_{12}, C_{13}, C_{22}, C_{23}, C_{33}, C_{44}, C_{55}, and C_{66}. In the orthorhombic elastic tensor matrix, there are three trivial eigenvalues, namely, C_{44}, C_{55}, and C_{66} which must be positive [34]. In an orthorhombic system, the necessary and sufficient Born criteria are given in Equation (2), while the elastic tensor values are given in Table 3 [34]:

$$\begin{gathered} C_{11} > 0, C_{11}C_{22} > C_{12}^2, \\ C_{11}C_{22}C_{33} + 2C_{12}C_{13}C_{23} - C_{11}C_{23}^2 - C_{22}C_{13}^2 - C_{33}C_{12}^2 > 0, \\ C_{44} > 0, C_{55} > 0, C_{66} > 0. \end{gathered} \tag{2}$$

In the orthorhombic crystal system, the bulk modulus B is related to the elastic constants C_{11}, C_{12}, C_{13}, C_{22}, C_{23} and C_{33}, through the following Equation (3), [35].

$$B = \frac{1}{3}(C_{11} + C_{22} + C_{33} + 2(C_{12} + C_{13} + C_{23})) \tag{3}$$

while on the other hand, the shear modulus, G is obtained from the elastic constants C_{44}, C_{55}, and C_{66} through Equation (4) given as

$$G = \frac{1}{5}(C_{44} + C_{55} + C_{66}) \tag{4}$$

The Voigt-Reuss-Hill [36–39] average mechanical properties for the orthorhombic Na_2CuP compound were computed from the elastic constants given in Table 3 using Equations (3) and (4). The bulk modulus B is a measure of the resistance to the changes in volume due to the application of uniform external pressure on a material. The results obtained for the B value for Na_2CuP were 32.4 GPa when using GGA-PBE, which shows that the material is soft because its bulk modulus is very low [40]. The measure of resistance of a material against deformation due to shear stress and strain is known as shear modulus, G. Shear modulus is a property useful for analysing torsional loading. The value obtained for G was 19.9 GPa for Na_2CuP, calculated using GGA-PBE.

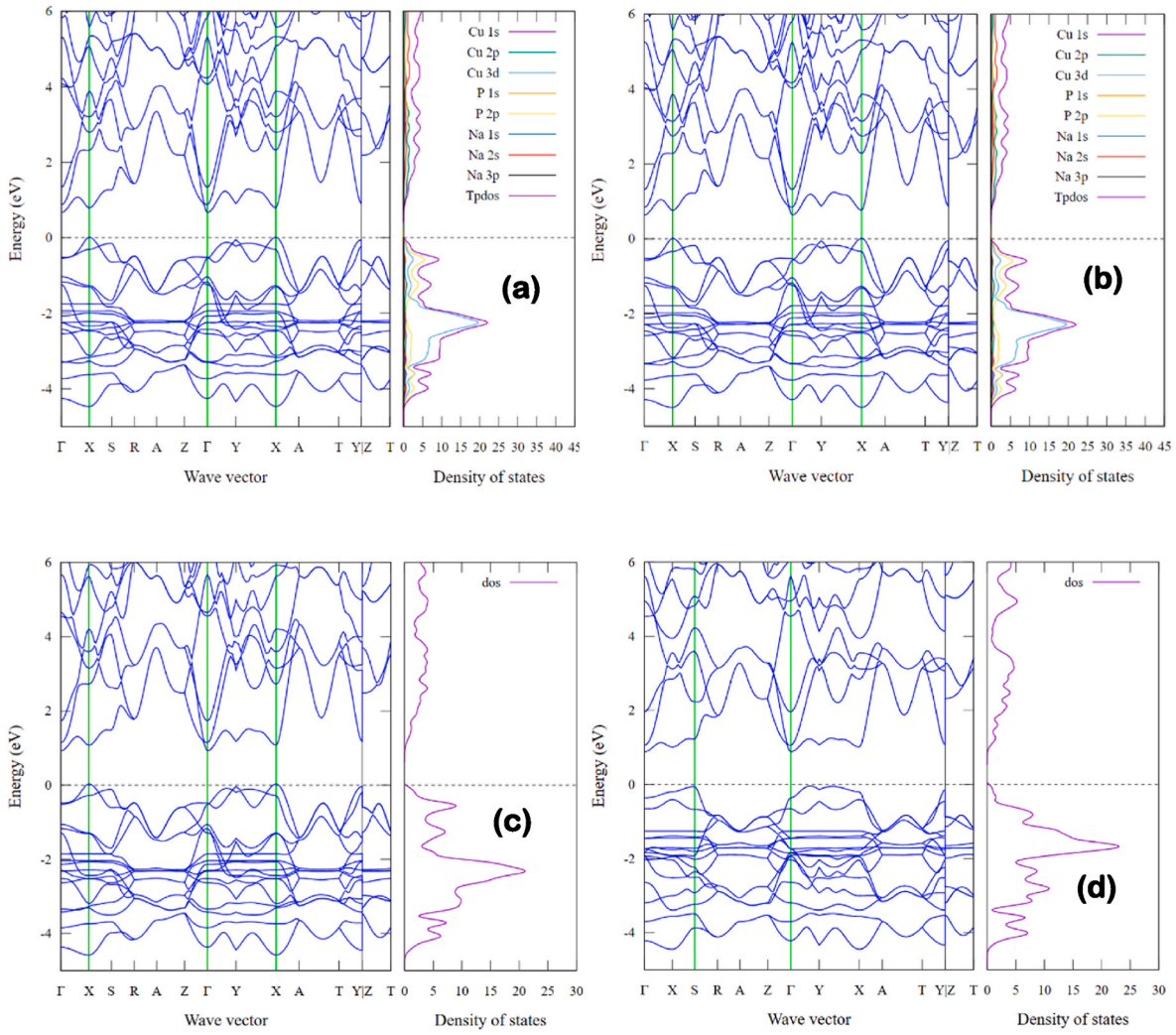

Fig. 3. The band structure of the Na_2CuP ternary compound and the projected density of states showing the band gaps and the band formation states for: (a) PBE-GGA 0.7848 eV, (b) WC-GGA 0.7523 eV, (c) SCAN-mGGA 1.084 eV, and (d) TB-mBJ-mGGA 1.084 eV.

Table 2
The summary of the electronic bandgaps of the Na_2CuP compound calculated using GGA-PBE, GGA-WC (Wu-Cohen), Machine Learning (ML), SCAN:mGGA, and TB-mBJ:mGGA.

	PBE	Wu-Cohen	ML	SCAN	TB-mBJ
This work	0.77 eV	0.75 eV	0.92 eV	1.084 eV	1.078 eV

The brittleness and ductility properties of a material can be determined from Pugh's [41] and Poisson's ratios [42]. Pugh's ratio is a dimensionless value obtained as the ratio of bulk modulus B to shear modulus G. A material is considered brittle if B/G is less than 1.75; otherwise, it is considered ductile if B/G is greater than 1.75. The values obtained in Table 4 using PBE-GGA show that Na_2CuP is brittle, which confirms the results reported elsewhere [20]. The type of bonding in a material is an intrinsic part of its mechanical properties. Poisson's ratio, n, can be used to determine whether a material has covalent or ionic bonding. A material is said to have covalent bonding if the value for Poisson's ratio is in the range $0 < n < 0.25$, while if the range lies at $0.25 < n < 0.5$, it is said to be ionic. According to the results shown in Table 4, the Na_2CuP compound was observed to have covalent bonding, which confirms a characteristic common in Zintl-phase materials. To predict whether the properties of a material are isotropic or anisotropic, the Kleinmann parameter ζ is used for computation. In the case of orthorhombic material which has three mutually perpendicular axes of

Table 4
The Voigt-Reuss-Hill average mechanical properties of Na_2CuP ternary compound. The bulk modulus B, Young's modulus E, Shear modulus G, Pugh's ratio B/G, Poisson's ratio n, and Debye temperature.

	B	E	G	B/G	n	ζ	θ_D (K)
PBE	32.4	49.4	19.9	1.63	0.2427	1.606	309.3
WC	34.6	53.0	21.3	1.62	0.2420	1.566	319.1

Table 3
Elastic tensor constants in GPa for Na_2CuP orthorhombic crystal system.

	C_{11}	C_{12}	C_{13}	C_{22}	C_{23}	C_{33}	C_{44}	C_{55}	C_{66}
PBE	73.15	8.67	6.91	67.95	30.80	59.21	36.69	11.91	11.73
WC	77.70	9.96	7.72	72.17	32.68	61.70	38.96	13.98	12.22

invariant length is given by Equation (5), [43]:

$$\zeta = \frac{C_{33}(C_{11} + C_{22}) - 2C_{23}^2}{C_{11}C_{22} - C_{23}^2} \quad (5)$$

A material is said to be isotropic if $\zeta = 1$ or anisotropic if $\zeta > 1$, for the case of Na_2CuP which has an orthorhombic structure, the Kleinmann parameters were predicted to be 1.606 and 1.566 using PBE-GGA and GGA-WC, respectively, showing that the material is anisotropic. The Debyes' temperature is another important parameter for evaluating material properties such as thermal expansion, thermal conductivity, crystal lattice vibration, melting point, and specific heat capacity of the material. The Debye temperature can be computed using Equation (6).

$$\theta_D = \left(\frac{h}{k_B}\right)\left[\frac{3n}{4\pi}\left(\frac{N_A\rho}{M}\right)\right]^{\frac{1}{3}} V_m \quad (6)$$

where V_m is the average sound velocity. The calculated θ_D for Na_2CuP was determined as 309.3 K and 319.1 K when using GGA-PBE and GGA-WC, respectively. Further, thermodynamic properties are discussed in the next section.

3.4. Debye properties

Debye properties are based on a theoretical model proposed by Peter Debye for describing the thermophysical properties of solids at finite temperatures. The model was proposed to aid in understanding the heat capacity of solids at low temperatures and the quantized lattice vibrations in crystal lattices. The Debyes' thermophysical properties of Na_2CuP ternary compound are depicted in Fig. 4. In Fig. 4(a), it shows the temperature-dependent variation of Debye's vibrational energy. In the Debye model, a solid-state material is treated as a continuous elastic medium and the vibrations of the atoms in the crystal lattice are approximated as sound waves [44–46]. The model assumes that the vibration of the atoms in the crystal lattice is harmonic analogous to waves in a continuous classical medium. Fig. 4(a) shows that the Debye vibrational energy was gradually increasing with the increasing temperature, the calculations agree well with the Debye model.

Debyes' model treats the vibrational energy as a sound wave. The vibrations are approximated as acoustic phonons with continuous frequency distribution up to a maximum frequency called the Debye frequency. The energy associated with the vibrational modes of the crystal lattice is given at a given temperature T. The negative Debye vibrational free energy arises due to the way the energy is distributed in the vibrational modes in the Debye model [44–46]. Fig. 4(b) shows the vibrational free energy of the Na_2CuP ternary compound where at 0 K up to approximately 250 K, the vibrational free energy is positive while beyond 250 K it assumes negative values, this shows that at low temperatures the energy levels of the materials are sparsely populated.

The Debye model is used for estimating the phonon contribution to the specific heat and the collective vibrations (phonons) of the entire crystal lattice. lattice entropy resulting from lattice vibration rises with increasing temperature as it is depicted in Fig. 4(c). The heat capacity is the measure of the amount of heat energy required to cause a change in temperature of a substance by a certain amount. A large heat capacity translates into high thermal conductivity and low thermal diffusivity in

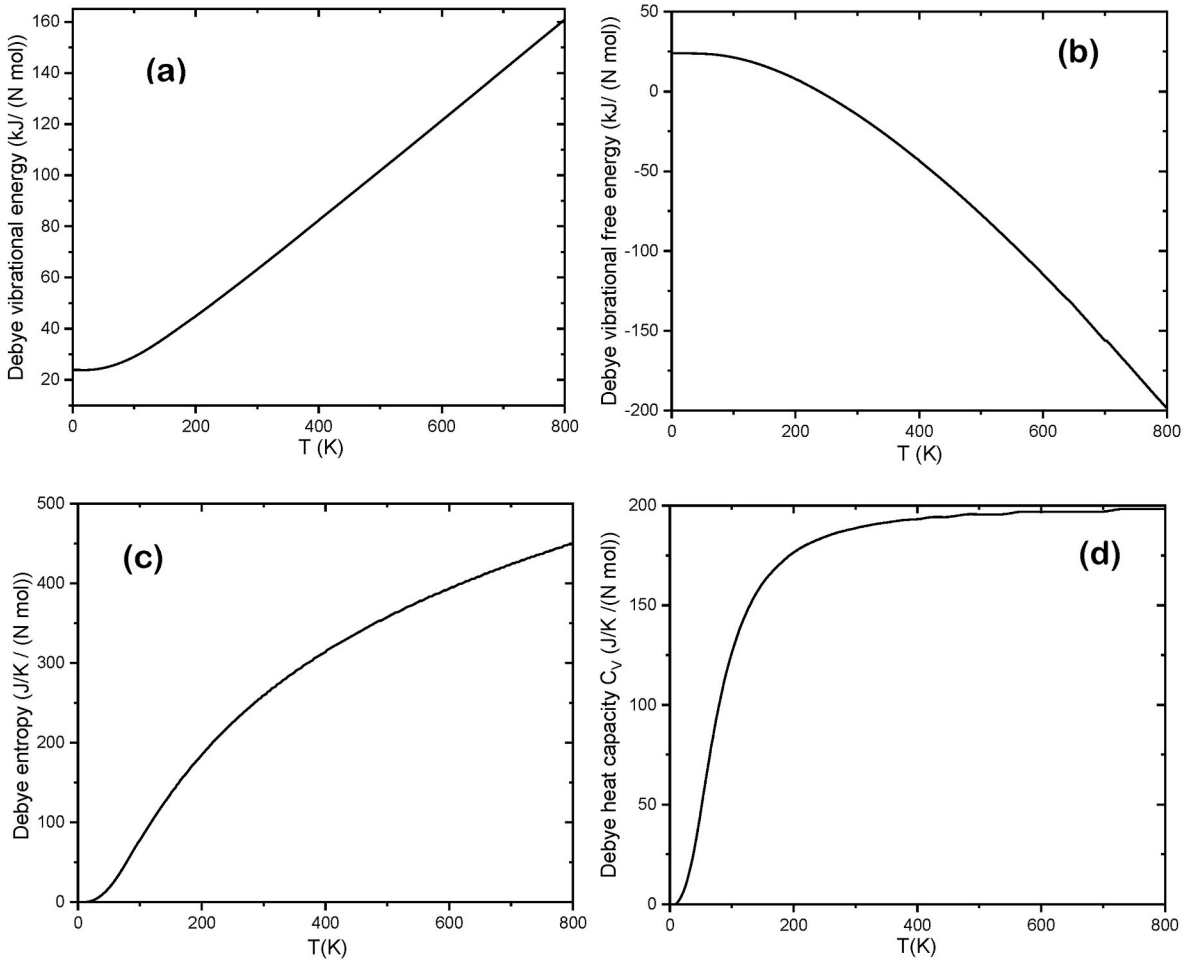

Fig. 4. The thermodynamics properties of the Na_2CuP ternary compound for: (a) Debye vibrational energy, (b) Debye vibrational free energy, (c) Debye entropy, and (d) Debye heat capacity.

a material. In the Debye model, the volumetric heat capacity is given in Equation (7) as;

$$C_V = \frac{d}{dT}\left(\frac{U}{N}\right) = 9R\left(\frac{T}{\theta_D}\right)^3 \int_0^{\frac{\theta_D}{T}} \frac{x^4 e^x}{(e^x - 1)} dx \quad (7)$$

where U is the internal energy of the solid material, N is the number of atoms in the solid, R is the gas constant, T is the temperature, θ_D is the Debye temperature, $x = \hbar\omega/K_B T$ is a dimensionless quantity where ω is the angular frequency of crystal lattice vibrational mode [44]. Fig. 4(d) shows the Debye heat capacity for the Na_2CuP ternary compound where it can be observed that the heat capacity increases rapidly before approaching almost a constant value, this behaviour corroborates what is predicted by the Debye model that the heat capacity approaches constant value after it has attained the materials Debye temperature, which had been calculated earlier in elastic constants calculation as $\theta_D = 319\,K$.

3.5. Optical properties

The optical properties reveal the interaction between matter and the incident electromagnetic wave spectra and the characteristic bandgap of the material being studied. In this work, a detailed description of the optical properties of the Na_2CuP ternary compound is presented with a frequency-dependent dielectric function using GGA-PBE. The dielectric function, known as the permittivity of the material, is described by a complex dielectric function consisting of two related parts, as given in Equation (8).

$$\varepsilon(\omega) = \varepsilon(\omega)_1 + j\varepsilon(\omega)_2 \quad (8)$$

In equation (8), $\varepsilon(\omega)_1 = n(\omega)^2 - k(\omega)^2$ is the real part composed of the refractive index $n(\omega)$ and extinction coefficient $k(\omega)$, while $\varepsilon(\omega)_2 = 2nk$ is the imaginary part of the dielectric function. The real part represents the generated polarisation owing to the interaction between the electromagnetic spectra and the material, and the imaginary part shows the ability of the material to attenuate the incident electromagnetic spectra. Fig. 5(a) shows the dielectric functions for the real and imaginary parts, where it is observed that the real part of the dielectric function has a strong dispersion signal from 0 eV to 3.4 eV then the dispersion assumes negative values from 3.4 eV–15 eV. In the cases where the values are negative, the photons of the electromagnetic wave spectra become completely attenuated, and the material is said to assert a metallic characteristic.

It can also be observed that the real part had a static value beyond 13.6 eV. On the other hand, the imaginary part of the dielectric functions shows a strong absorption peak between 1.1 eV – and 6.6 eV, thereafter, the signal monotonically decreases gradually. The section occupied by the strong absorption signal is the infrared to the ultraviolet region of the spectrum, which shows that the Na_2CuP material may be suitable for applications in photovoltaic devices such as solar cells.

The refractive index and extinction coefficient patterns of the studied

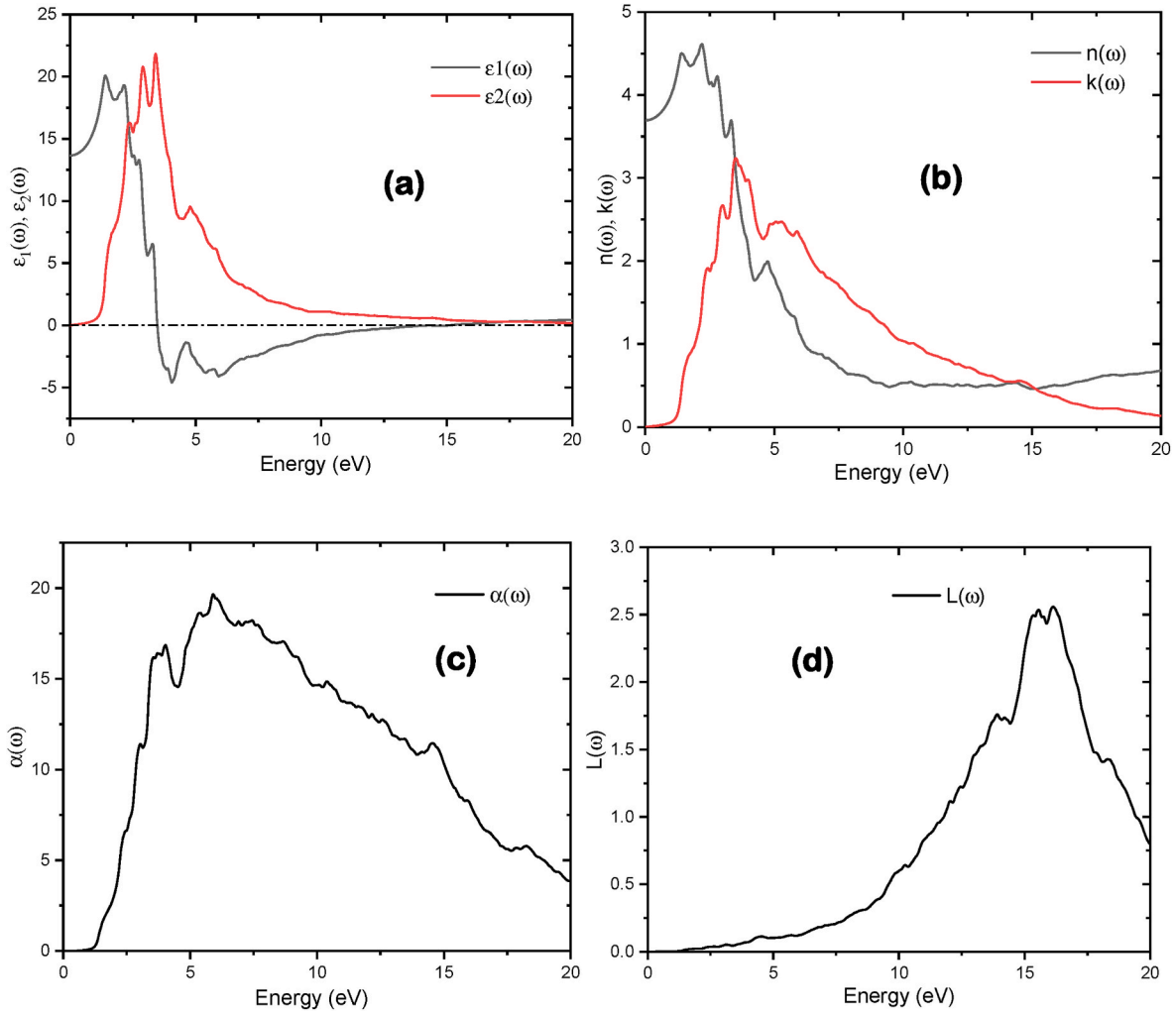

Fig. 5. Optical properties of Na_2CuP ternary compound showing (a) dielectric constants epsilon 1 and epsilon 2, (b) frequency-dependent refractive index and extinction coefficient, (c) frequency-dependent absorption coefficient, and (d) frequency-dependent energy loss function.

material are shown in Fig. 5(b) as a function of energy in the range of 0–20 eV which represents the deep ultraviolet to infrared regions of the electromagnetic wave spectrum. The refractive index of the materials forms a dispersion of the incident electromagnetic wave spectrum. The refractive index describes the refraction factor of the material at different wavelengths of the spectrum, whereas the extinction coefficient describes the attenuation or extent of absorption of the incident photons at different wavelengths.

The extinction coefficient is related to the absorption coefficient by $4\pi k/\lambda$ where λ is the wavelength of the incident electromagnetic wave spectra. The refractive index is closely related to the real part of the dielectric constant $\varepsilon(\omega)_1$. Moreover, it can be observed that the static values of the refractive index to that of the real part of the dielectric constant agree very well with their well-known relationship which is $\varepsilon(0)_1 = n(0)^2$. The refractive index revealed strong dispersion between the 0–8.2 eV region of the spectra and a monotonic decrease beyond 8.2 eV. The refractive index value of Na_2CuP material was obtained as 3.7. The extinction coefficient represents the extent of absorption of the incident light photons by a material; the higher the value, the higher the absorption, and vice versa. The extinction coefficient signal for Na_2CuP starts at approximately 1.15 eV, it then rapidly increases to its maximum point at 4.15 eV and then decreases gradually up to the end of the spectrum at 20 eV.

The optical absorption coefficient is the measure of the amount of light a medium absorbs. The absorption coefficient depends on the particular material and wavelength, meaning that the higher the absorption coefficient, the higher the absorption by the material at that particular wavelength. Fig. 5(c) shows the absorption characteristics of Na_2CuP, where the absorption coefficient spectrum is almost identical to that of the extinction coefficient. The Na_2CuP material was observed to possess a strong absorption between 1.15 eV and 15 eV, and beyond 15 eV, it still showed a substantial amount of absorption. The absorption coefficient characteristics support an earlier observation that Na_2CuP is an excellent material for photovoltaics.

The energy-loss function describes the amount of energy lost by the incident photons of the electromagnetic wave after interacting with the material. The energy loss may take different forms, either through the excitation of collective electron excitations such as plasmons or interband transitions. Information revealed by the energy loss function is crucial for studying the electronic structure and optical properties of a material. Fig. 5(d) shows the energy-loss function of Na_2CuP as a function of energy. This shows that the material had a higher energy loss at higher energies and vice versa.

Optical reflectivity occurs when the incident electromagnetic wave spectra or the photons interact with the material. Some photons are absorbed, while others are transmitted through or reflected. Reflectivity can vary depending on the type of material used, such as a good conductor, lossless dielectric, or lossy dielectric. Fig. 5(e) shows the reflectivity characteristics of the Na_2CuP ternary semiconductor. It can be observed that the reflectivity and energy loss spectra are opposite to each other; in the spectral section where reflectivity is strong, the energy loss is lower, and vice versa.

4. Conclusions

The Zintl-phased Na_2CuP compound has been determined to be a semiconductor material with its bandgap predicted to be 0.7523 eV and 0.7848 eV using generalised gradient approximation with Wu-Cohen and Perdew-Burke-Ernzerhof functionals, respectively. The bandgap was re-approximated using metaGGA functionals as 1.078 eV and 1.084 eV using Tran-Blaha modified Berke Johnson (TB-mBJ) and SCAN functionals, respectively. The projected density of states using the GGA revealed that the conduction band formation was mainly by Cu 2*p*, P 2*p*, and Na 2*s* orbitals with the rest of the orbitals making a minor contribution, whereas the valence band formation was mainly formed by Cu 3*d* and P 2*p*, with the rest of the orbital playing a minor role in the formation. The Na_2CuP material was found to be mechanically brittle with a covalent bond, which is a characteristic of Zintl-phased materials. The thermodynamic properties support the findings of the mechanical properties of the material and agree with the Debye model. The Na_2CuP material was observed to strongly absorb light in the 1.15 eV–15 eV energy region, portraying its suitability for photovoltaic applications.

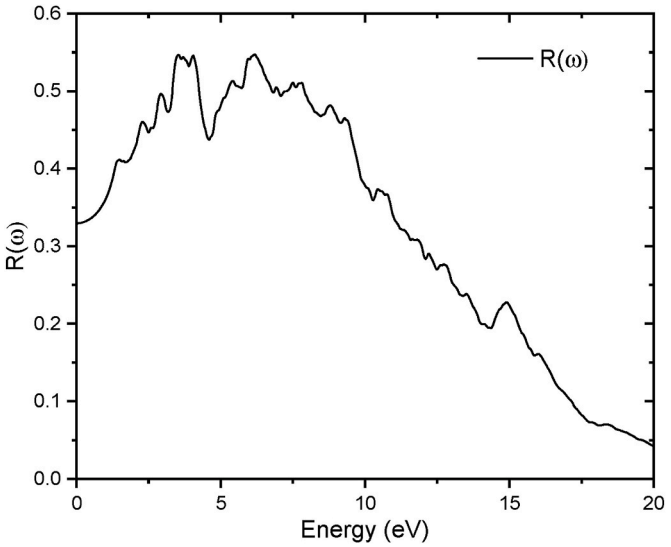

Fig. 5(e). The frequency-dependent reflectivity of Na_2CuP ternary compound.

CRediT authorship contribution statement

Robinson Musembi: Writing – review & editing, Writing – original draft, Visualization, Validation, Supervision, Software, Resources, Project administration, Methodology, Investigation, Funding acquisition, Formal analysis, Data curation, Conceptualization. **Mwende Mbilo:** Writing – review & editing, Validation, Investigation, Formal analysis, Data curation. **Martin Nyamunga:** Writing – review & editing, Validation, Methodology, Investigation, Formal analysis, Data curation. **John Kachila:** Writing – review & editing, Validation, Investigation, Formal analysis, Data curation.

Declaration of competing interest

The authors declare that they have no known competing financial interests or personal relationships that could have appeared to influence the work reported in this paper.

Data availability

Data will be made available on request.

Acknowledgements

The authors acknowledge RSIF grant number RSIF_RA_015 for support, the International Science Programme for Computational Seed Grant through the KEN02 grant, and the Centre for High-Performance Computing CHPC-RSA for computing resources. MM acknowledge the Partnership for Skills in Applied Sciences, Engineering and Technology (PASET) - Regional Scholarship Innovation Fund (RSIF) for the Funding opportunity, and the L'Oréal-UNESCO For Women in Science Sub-Saharan Africa Young Talents Programme for endowment award.

References

[1] K. Sopian, S.L. Cheow, S.H. Zaidi, "An overview of crystalline silicon solar cell technology: past, present, Future Times (2017) 020004, https://doi.org/10.1063/1.4999854.

[2] C. Battaglia, A. Cuevas, S. De Wolf, High-efficiency crystalline silicon solar cells: status and perspectives, Energy Environ. Sci. 9 (5) (2016) 1552–1576, https://doi.org/10.1039/C5EE03380B.

[3] S. Kim, V.Q. Hoang, C.W. Bark, Silicon-based technologies for flexible photovoltaic (PV) devices: from basic mechanism to manufacturing technologies, Nanomaterials 11 (11) (Nov. 2021) 2944, https://doi.org/10.3390/nano11112944.

[4] G.K. Gupta, R. Chaurasiya, A. Dixit, Thermodynamic stability and optoelectronic properties of Cu(Sb/Bi)(S/Se)$_2$ ternary chalcogenides: promising ultrathin photo absorber semiconductors, Sol. Energy 177 (Jan. 2019) 679–689, https://doi.org/10.1016/j.solener.2018.11.064.

[5] P. Mariyappan, M.G.M. Pandian, T.H. Chowdhury, S.M. Babu, S. Subashchandran, Investigations on the stability of the ambient processed bismuth based lead-free $A_3Bi_2I_9$ (A = MA; Cs) perovskite thin-films for optoelectronic applications, Mater. Sci. Eng., B 297 (Nov. 2023) 116706, https://doi.org/10.1016/j.mseb.2023.116706.

[6] J. Nover, R. Zapf-Gottwick, C. Feifel, M. Koch, J.H. Werner, Leaching via weak spots in photovoltaic modules, Energies 14 (3) (Jan. 2021) 692, https://doi.org/10.3390/en14030692.

[7] S. Fang, et al., Zintl chemistry: current status and future perspectives, Chem. Eng. J. 433 (Apr) (2022), https://doi.org/10.1016/j.cej.2021.133841.

[8] S. Wafula, R. Musembi, F. Nyongesa, Analysis of K_4ZnAs_2 Zintl phased ternary semiconductor compound for optoelectronic application, Results in Materials 20 (Dec. 2023) 100469, https://doi.org/10.1016/J.RINMA.2023.100469.

[9] S. Baranets, A. Ovchinnikov, S. Bobev, Structural diversity of the Zintl pnictides with rare-earth metals, in: Handbook on the Physics and Chemistry of Rare Earths vol 60, 2021, https://doi.org/10.1016/bs.hpcre.2021.07.001.

[10] A. Bekhti-Siad, et al., Electronic, optical and thermoelectric investigations of Zintl phase AE_3AlAs_3 (AE = Sr, Ba): first-principles calculations, Chin. J. Phys. 56 (3) (Jun. 2018) 870–879, https://doi.org/10.1016/j.cjph.2018.03.022.

[11] A. Ovchinnikov, S. Bobev, Zintl phases with group 15 elements and the transition metals: a brief overview of pnictides with diverse and complex structures, J. Solid State Chem. 270 (Feb. 2019) 346–359, https://doi.org/10.1016/j.jssc.2018.11.029.

[12] A. Ovchinnikov, S. Bobev, Data from the electronic band structures of several Zintl phases with group 15 elements and the transition metals, Data Brief 22 (Feb. 2019) 446–450, https://doi.org/10.1016/j.dib.2018.12.040.

[13] D.S. Jayalakshmi, T. Hrisheekesan, G. Akshaya, D. Hemanand, W.T. Chembian, P. Arun Prakash, Computational investigation of optical, thermal and thermoelectric properties of Cs $_3$ P compound, J Phys Conf Ser 1979 (1) (Aug. 2021) 012055, https://doi.org/10.1088/1742-6596/1979/1/012055.

[14] M. Irfan, S. Azam, A. Iqbal, Proposal of new stable ABC_2 type ternary semiconductor pnictides $K_3Cu_3P_2$ and $K_3Ni_3P_2$: first-principles calculations and prospects for thermophysical and optoelectronic applications, Int. J. Energy Res. 45 (2) (Feb. 2021) 2980–2996, https://doi.org/10.1002/er.5992.

[15] M. Mbilo, R. Musembi, First-principles calculation to investigate the structural, electronic, elastic, mechanical, and optical properties of K_2NiP_2ternary compound, AIP Adv. 12 (10) (2022), https://doi.org/10.1063/5.0118809.

[16] Y. Prots, U. Aydemir, S.S. Öztürk, M. Somer, Crystal structure of tetrapotassium diarsenidozincate, K_4ZnAs_2, Z. Kristallogr. N. Cryst. Struct. 222 (3) (Sep. 2007) 163–164, https://doi.org/10.1524/ncrs.2007.0067.

[17] B. Eisenmann, M. Somer, Intermetallische Verbindungen mit $HgCl_2$ -isosteren Anionen: Strukturelle und schwingungsspektroskopische Untersuchung von Na_4HgP_2, K_4ZnP_2 , K_4CdP_2 und K_4HgP_2, Z. Naturforsch. B Chem. Sci. 44 (10) (Oct. 1989) 1228–1232, https://doi.org/10.1515/znb-1989-1015.

[18] M. Mbilo, G.S. Manyali, R.J. Musembi, Ab initio study of $K_3Cu_3P_2$ material for photovoltaic applications, Computational Condensed Matter 32 (Sep. 2022) e00726, https://doi.org/10.1016/J.COCOM.2022.E00726.

[19] G. Ding, T. Sun, G. Surucu, O. Surucu, A. Gencer, X. Wang, Complex nodal structure phonons formed by open and closed nodal lines in CoAsS and Na_2CuP solids, Phys. Chem. Chem. Phys. 24 (28) (2022) 17210–17216, https://doi.org/10.1039/D2CP01992B.

[20] Fella Daghor, S. Maabed, On the yet Not Explored Physical Properties of the Ternary Polar Intermetallic Compounds Na_2CuP and Na_2CuAs : a Prediction Study by DFT, Amar Talidji University, Laghouat, 2019.

[21] D. Dahliah, G. Brunin, J. George, V.-A. Ha, G.-M. Rignanese, G. Hautier, High-throughput computational search for high carrier lifetime, defect-tolerant solar absorbers, Energy Environ. Sci. 14 (9) (2021) 5057–5073, https://doi.org/10.1039/D1EE00801C.

[22] Kh Kabita, B.I. Sharma, First-principles study on structural, phase transition and electronic structure of Zinc Sulfide (ZnS) within LDA, GGA and mBJ potential, J Phys Conf Ser 759 (Oct. 2016) 012029, https://doi.org/10.1088/1742-6596/759/1/012029.

[23] P. Giannozzi, et al., Quantum ESPRESSO: a modular and open-source software project for quantum simulations of materials, J. Phys. Condens. Matter 21 (39) (Sep. 2009) 395502, https://doi.org/10.1088/0953-8984/21/39/395502.

[24] P. Giannozzi, et al., Advanced capabilities for materials modelling with Quantum ESPRESSO, J. Phys. Condens. Matter 29 (46) (Nov. 2017) 465901, https://doi.org/10.1088/1361-648X/aa8f79.

[25] J.P. Perdew, K. Burke, M. Ernzerhof, Generalized Gradient Approximation Made Simple, 1996.

[26] E. Gossett, et al., AFLOW-ML: a RESTful API for machine-learning predictions of materials properties, Comput. Mater. Sci. 152 (Sep. 2018) 134–145, https://doi.org/10.1016/j.commatsci.2018.03.075.

[27] V. Stanev, et al., Machine learning modelling of superconducting critical temperature, npj Comput. Mater. 4 (1) (Jun. 2018) 29, https://doi.org/10.1038/s41524-018-0085-8.

[28] F. Legrain, J. Carrete, A. van Roekeghem, S. Curtarolo, N. Mingo, How chemical composition alone can predict vibrational free energies and entropies of solids, Chem. Mater. 29 (15) (Aug. 2017) 6220–6227, https://doi.org/10.1021/acs.chemmater.7b00789.

[29] O. Isayev, C. Oses, C. Toher, E. Gossett, S. Curtarolo, A. Tropsha, Universal fragment descriptors for predicting properties of inorganic crystals, Nat. Commun. 8 (1) (Jun. 2017) 15679, https://doi.org/10.1038/ncomms15679.

[30] G. Kresse, D. Joubert, From ultrasoft pseudopotentials to the projector augmented-wave method, Phys. Rev. B 59 (3) (Jan. 1999) 1758–1775, https://doi.org/10.1103/PhysRevB.59.1758.

[31] G. Savelsberg, H. Schäfer, Darstellung und Kristallstruktur von Na_2CuP, K_2AgAs, K_2AgSb und K_2AgBi, Zeitschrift fur Naturforschung - Section B Journal of Chemical Sciences 32 (7) (Jul. 1977) 745–748, https://doi.org/10.1515/ZNB-1977-0704.

[32] C. Chen, et al., Suppressing thermal tail by Dirac states and high density of states in two-dimensional Ag_2S toward low-power electronics, ACS Mater. Lett. 6 (5) (May 2024) 2065–2071, https://doi.org/10.1021/acsmaterialslett.4c00296.

[33] J. Yang, et al., Extreme anisotropic dispersion and one-dimensional confined electrons in 2-D SiP_2 FETs with high transmission coefficients, IEEE Trans Electron Devices 70 (3) (Mar. 2023) 1330–1337, https://doi.org/10.1109/TED.2022.3232756.

[34] F. Mouhat, F.-X. Coudert, Necessary and sufficient elastic stability conditions in various crystal systems, Phys. Rev. B 90 (22) (Dec. 2014) 224104, https://doi.org/10.1103/PhysRevB.90.224104.

[35] Z. Ye, F. Jia, S. Xu, D. Elliston, H. Su, W. Ren, First-principles study of the structural and elastic properties of orthorhombic rare-earth aluminates $RAlO_3$ (R = Sm–Lu), J. Mater. Res. 39 (6) (Mar. 2024) 903–912, https://doi.org/10.1557/s43578-023-01279-0.

[36] D.H. Chung, W.R. Buessem, The voigt-reuss-hill approximation and elastic moduli of polycrystalline MgO, CaF_2, β-ZnS, ZnSe, and CdTe, J. Appl. Phys. 38 (6) (May 1967) 2535–2540, https://doi.org/10.1063/1.1709944.

[37] R. Hill, The elastic behaviour of a crystalline aggregate, Proc. Phys. Soc. 65 (5) (May 1952) 349–354, https://doi.org/10.1088/0370-1298/65/5/307.

[38] A. Reuss, Calculation of the yield point of mixed crystals based on the plasticity condition for single crystals, ZAMM - Journal of Applied Mathematics and Mechanics/Z. Angew. Math. Mech. 9 (1) (Jan. 1929) 49–58, https://doi.org/10.1002/zamm.19290090104.

[39] W. Voigt, Textbook of Crystal Physics, Vieweg+Teubner Verlag, Wiesbaden, 1966, https://doi.org/10.1007/978-3-663-15884-4.

[40] M.L. Cohen, Theory of bulk moduli of hard solids, Materials Science and Engineering: A 105–106 (Nov. 1988) 11–18, https://doi.org/10.1016/0025-5416(88)90475-2.

[41] H. Liu, S. Tang, Y. Ma, W. Liu, C. Liang, Short-range ordering governs brittleness and ductility in W-Ta solid solution: insights from Pugh's shear-to-bulk modulus ratio, Scr Mater 204 (Nov. 2021) 114136, https://doi.org/10.1016/j.scriptamat.2021.114136.

[42] G.N. Greaves, A.L. Greer, R.S. Lakes, T. Rouxel, Poisson's ratio and modern materials, Nat. Mater. 10 (11) (Nov. 2011) 823–837, https://doi.org/10.1038/nmat3134.

[43] A. Bakar, A.O. Alrashdi, M.M. Fadhali, A. Afaq, H.A. Yakout, M. Asif, Effect of pressure on structural, elastic and mechanical properties of cubic perovskites $XCoO_3$ (X = Nd, Pr) from first-principles investigations, J. Mater. Res. Technol. 19 (Jul. 2022) 4233–4241, https://doi.org/10.1016/J.JMRT.2022.06.126.

[44] H. Zhong, J. Lonergan, J.S. McCloy, S.P. Beckman, The thermophysical properties of TcO_2, Crystals 14 (3) (Feb. 2024) 228, https://doi.org/10.3390/cryst14030228.

[45] P. Li, J. Chen, L. Huang, J. Zhang, First-principles study of structural, mechanical, electronic properties and Debye temperature of $NbCo_2$ Laves phases under pressure, Physica B Condens Matter 676 (Mar. 2024) 415683, https://doi.org/10.1016/J.PHYSB.2024.415683.

[46] C.R. Xu, L. Shao, N. Ding, H.H. Jiang, B.Y. Tang, Study of thermal properties of TiCNO by Debye-Einstein model and Debye-Grüneisen model, Mater. Today Commun. 38 (Mar. 2024) 107918, https://doi.org/10.1016/J.MTCOMM.2023.107918.